A 0.9-V 60-μW 1-Bit Fourth-Order Delta-Sigma Modulator With 83-dB Dynamic Range

Jeongjin Roh, *Member, IEEE*, Sanho Byun, Youngkil Choi, *Student Member, IEEE*,
Hyungdong Roh, *Student Member, IEEE*, Yi-Gyeong Kim, and Jong-Kee Kwon, *Member, IEEE*

Abstract—A 0.9-V 60-μW delta-sigma modulator is designed using standard CMOS 0.13-μm technology. The modulator achieves 83-dB dynamic range in a signal bandwidth of 20 kHz with a sampling frequency of 2 MHz. The input-feedforward architecture is used to reduce the voltage swing of the integrators, which enables low-power amplifiers. By considering the characteristics of the modulator architecture, low-quiescent operational transconductance amplifiers are designed, which use positive feedback to increase dc gain. The designed modulator shows very high figure of merit among the state-of-the-art sub-1-V modulators.

Index Terms—Low power, low voltage, operational transconductance amplifier, sigma-delta modulation, switched capacitator circuits.

I. INTRODUCTION

THE design of low-voltage low-power delta-sigma data converters has been an important academic and industrial issue for more than a decade [1]. Recently, the proliferation of battery-operated systems has demanded even more power-efficient circuits than ever. Sub-1-V delta-sigma modulators have been presented in many papers [2]–[6], and our work shows a 0.9-V design with only 60 μW for the 83-dB dynamic range. A common technique for low-voltage design is to use charge pumps to generate higher voltage than the supply voltage for switches [7], [13]. Another popular technique is the switched-op amp instead of charge pumps [2], [3].

However, a recent process development has enabled low-threshold voltage transistors for modulator design [8], [9], which eliminate the need for charge pumps or switched-op amps. We used low-threshold voltage devices of a 0.13-μm CMOS process, and this enables a simple circuit design, which in turn enables a more power-efficient modulator. We also exploit the advantage of the feedforward modulator for low-power circuit design. Feedforward modulator architecture has gained popularity recently because of the small voltage swings in the loop filter of the modulator. This allows extra room for more efficient circuit design. By combining the advantages of feedforward architecture and the low-power operational transconductance amplifier (OTA), the implemented

modulator achieves very high figure-of-merit (FOM) among the state-of-the-art modulators.

Section II discusses the details of the architectural issues for low-power design. The effect of the parasitic integrator caused by the parasitic capacitance at the input node of the comparator is analyzed, the leakage current issue is addressed, and the requirements of the OTA specifications are discussed. Section III then shows the circuit blocks used in the modulator. Details of the circuit design are provided in this section. Section IV has measurement results and is followed by the conclusion.

II. ARCHITECTURAL DESIGN

In this section, architectural and circuit design issues will be discussed for low-power circuit design. First, the design of modulator topology is explained. The effect of the feedforward topology for low-power design is analyzed. The architectural issue and leakage current are discussed. The design requirement of an OTA is also presented that considers the property of the feedforward topology.

A. Modulator Topology

Most of the low-voltage modulators have been implemented using feedback architectures. Instead of the feedback architecture, our design employs the input-feedforward architecture, which has become popular in recent years [10]–[12].

The feedforward architecture has an extra signal path from the input of the modulator to the quantizer. This simple architectural modification can have significant impact on analog circuit design.

The signal component, which appears in the loop filter of the conventional modulator, is completely removed in the feedforward modulator. This feature makes the feedforward architecture very attractive. The analog circuits do not need to have large voltage swings, so the design requirement of the OTA becomes relaxed. We have used this feature to design a very low-power modulator, as explained in Sections II-B–E and III.

There should be several important choices in designing a delta-sigma modulator architecture. The order of a modulator, the oversampling ratio, the choice between a single-loop or cascaded modulator, and the choice between a single-bit or multibit quantizer are all important decisions to make [13], [14]. Our design goal is to design a highly power-efficient modulator, and it is realized that complex modulator architecture would require high power to make it function properly. For example, cascaded modulators require more stringent analog components such as high-performance OTAs. Multibit architecture requires the dynamic element matching (DEM) technique, which also requires extra current consumption for the extra
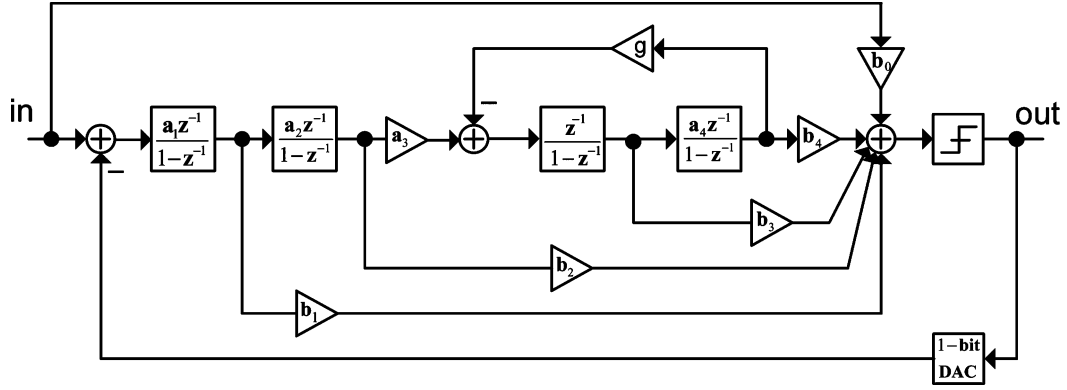
Fig. 1.   Single-loop fourth-order topology.

blocks. Therefore, the modulator in this paper is designed as a single-loop single-bit architecture. The modulator is selected to have fourth-order with an oversampling ratio of 50 as a design optimization after intensive behavioral simulations.

Fig. 1 shows the designed single-loop fourth-order topology with its feedback and feedforward coefficients. The feedforwarded paths are all summed at the input node of a comparator. The NTF of the designed modulator can be calculated as

$$\text{NTF}(z) = \frac{A(z)}{B(z)} = \frac{A_4 Z^4 + A_3 Z^3 + A_2 Z^2 + A_1 Z^1 + A_0}{B_4 Z^4 + B_3 Z^3 + B_2 Z^2 + B_1 Z^1 + B_0}$$
(1)

where

$$A_4 = 1$$
$$A_3 = -4$$
$$A_2 = 6 + a_4 g$$
$$A_1 = -4 - 2a_4 g$$
$$A_0 = 1 + a_4 g$$
$$B_4 = 1$$
$$B_3 = -4 + a_1 b_1$$
$$B_2 = 6 + a_4 g - 3a_1 b_1 + a_1 a_2 b_2$$
$$B_1 = -4 - 2a_4 g + 3a_1 b_1 - 2a_1 a_2 b_2 + a_1 a_4 b_1 g + a_1 a_2 a_3 b_3$$
$$B_0 = (1 + a_4 g)(1 - a_1 b_1 + a_1 a_2 b_2) + a_1 a_2 a_3 (a_4 b_4 - b_3).$$

The local feedback loop with a gain coefficient of g, which forms a resonator, is to move a pair of the NTF zeros to the edge of the signal band. The coefficients of the designed modulator are summarized in Table I. The ideal output spectrum of a behavioral simulation is shown in Fig. 2 with these coefficients. It clearly shows a notch in the spectrum caused by the resonator.

B. Effect of the Parasitic Capacitance of the Comparator

The feedforwarded integrator outputs are summed at the comparator input node with proper switch clocking. The parasitic capacitor at the input node of the comparator stores the summation output during the comparator's evaluation time. Then the stored charge is summed with the feedforwarded voltages at the next clock to determine the comparator output. The capacitor at the input node of the comparator combined

TABLE I
MODULATOR COEFFICIENTS

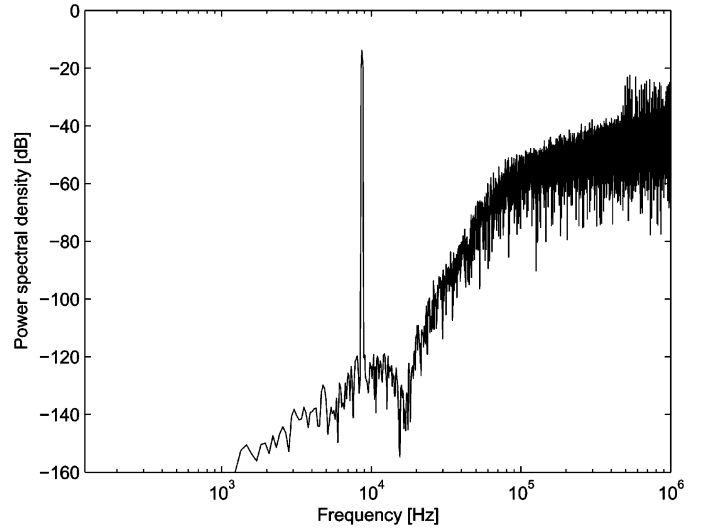| Integrator coefficients	Feedforward coefficients	Resonator coefficients
	$b_0 = 1.0$	
$a_1 = 0.2$	$b_1 = 4.0$	$g = 1/36$
$a_2 = 0.5$	$b_2 = 3.0$	
$a_3 = 0.44$	$b_3 = 1.5$	
$a_4 = 0.1$	$b_4 = 1.5$	

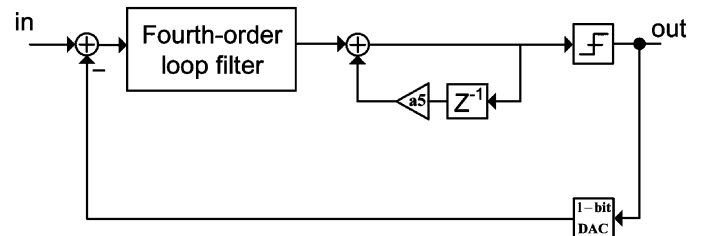Fig. 2.   Ideal output spectrum with a 8.7-kHz input signal.

Fig. 3.   Modulator with the effect of the parasitic capacitor at the input node of the comparator.

with the switch forms the parasitic fifth integrator as shown in Fig. 3. The integrator coefficient a_5 is determined by the ratio of the parasitic capacitance to the total capacitance at the comparator input node. This parasitic integrator has the benefit of
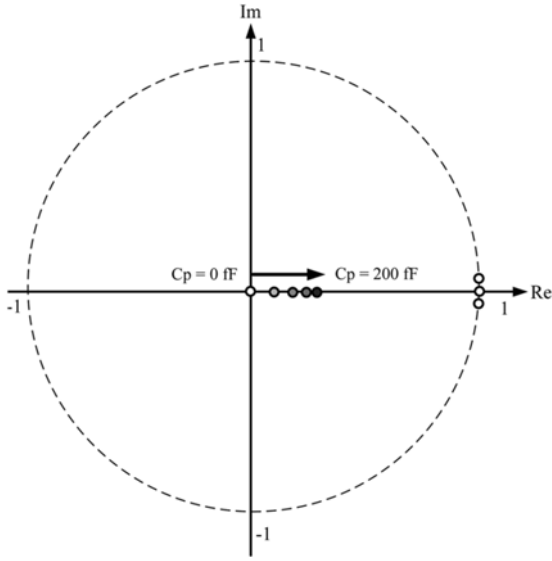
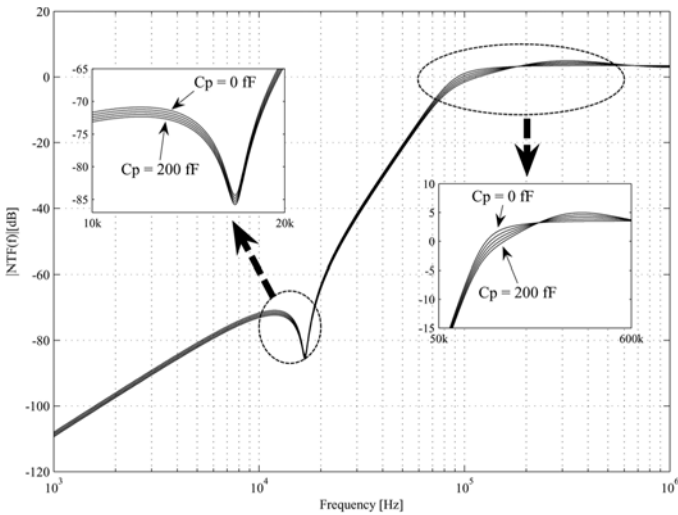Fig. 4. Movement of the fifth zero of NTF with different parasitic capacitors. (0, 50, 100, 150, and 200 fF).

Fig. 5. Variation of NTF with different parasitic capacitors.

Fig. 6. Integrator output swings with a 8.7-kHz half-scale input signal.
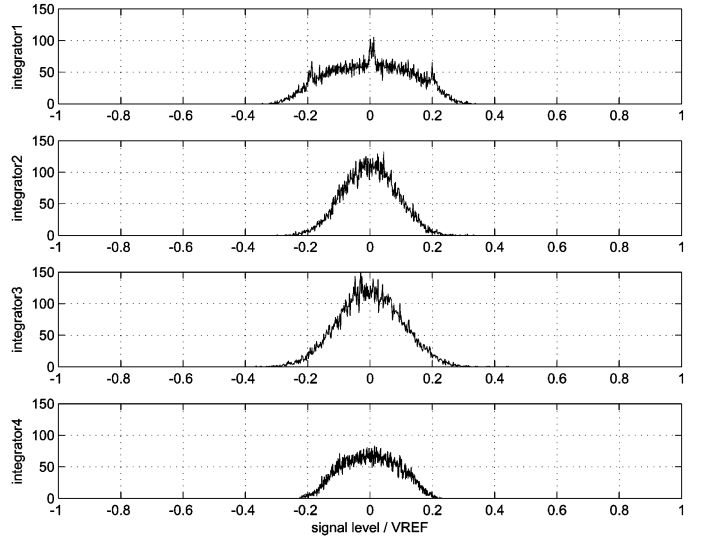
Fig. 7. Histogram of the integrator output swings.

increasing the noise shaping property by increasing the order of the modulator from four to five.

$$\text{NTF}_{\text{new}}(z) = \text{NTF}(z) \times \frac{B(z)(z - a_5)}{B(z)z - A(z)a_5} \qquad (2)$$

The analysis of the modulator in Fig. 3 shows that the new NTF in (2) is different from (1), where $a_5 = C_p/C_{\text{total}}$, C_p is the parasitic capacitance, and the C_{total} is the total capacitance at the comparator input node including C_p. The locations of the original four zeros are fixed while the locations of the poles change. The location of the extra fifth zero is determined by the size of parasitic capacitor. Fig. 4 shows that the movement of fifth zero. If there is no parasitic capacitor, the NTF is same as that of the fourth-order modulator, as expected. However, the fifth zero moves to the right on the real axis as the parasitic capacitance increases. This extra zero has the benefit
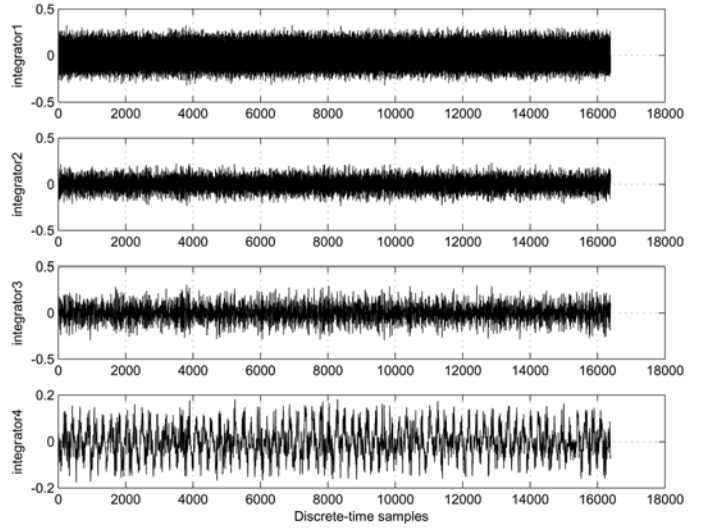
of increased noise-shaping action as shown in Fig. 5. The attenuation of the quantization noise in the signal band is slightly increased.

A concern about the parasitic capacitor is the stability of the modulator. The modulator becomes a fifth-order system by the parasitic integrator, and the stability problem can arise. The NTF peak value increases from 1.5 to 1.8 as the parasitic capacitance increases from 0 to 200 fF. If the NTF peak increases too much, the feedback system can become unstable [14]. In our design, the estimated total capacitance is less than 100 fF, which does not affect the stability.

C. Integrator Output Swings

Since the presented modulator is optimized to use the feature of low-voltage swing at the input of the loop filter, it is essential to watch the voltage swings at the outputs of the integrators. A behavioral simulation with a half-scale input signal is performed to show the integrator output swings as in Figs. 6 and 7. The figures show scaled output swings to the full-scale reference
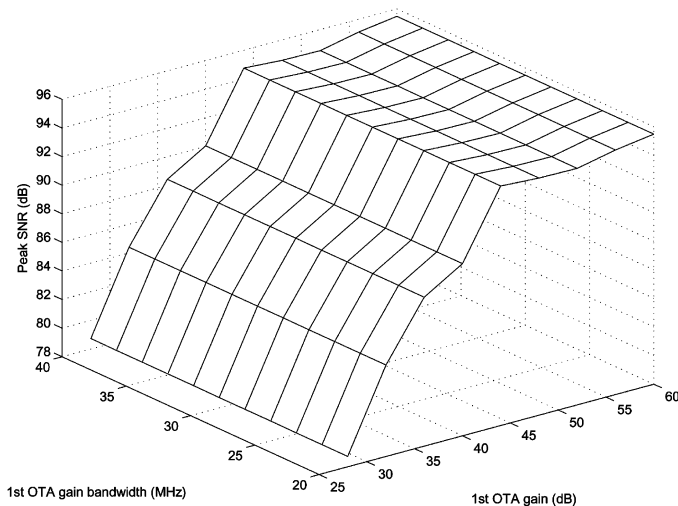
Fig. 8. SNR versus gain and bandwidth variations.

voltage. As can be seen from the figures, the largest output swing is observed at the first integrator, but it is still within less than 30% of the reference voltage. This enables the OTA, which is a key component in the integrator, to have relaxed requirements, as previously noted. For example, the OTA's output headroom requirement is relaxed, and a high slew rate is not required. More details of the circuit design are discussed in Section III.

D. OTA Requirements

As mentioned in the previous section, the integrator voltage swing of the designed modulator is limited to a narrow range. Therefore, the OTAs do not need to respond to large signal changes. This feature is important in designing low-voltage modulators since slewing becomes a noncritical requirement of the OTA; thus low-quiescent current would be sufficient.

Another important design consideration is the tolerance of the modulator for the process variations. Since the unavoidable process variations cause circuit performance fluctuations, the analog circuits must have sufficient margins for the variations. Since the first OTA has a dominant impact on the modulator's performance, the effect of the first OTA's functional variation is simulated. Fig. 8 shows the SNR degradation due to the OTA gain and bandwidth variations. The figure shows that the wide variation does not affect the SNR significantly. If the gain is above 45 dB, the modulator's SNR does not degrade. The SNR starts to fall below 90 dB if the OTA gain becomes lower than 42 dB. This simulation result is not surprising since previous research already proved it [9], [14].

E. Switches and Leakage Current

Switches are the key element in switched-capacitor circuits. CMOS technology has been the dominant choice to implement switched-capacitor circuits since it does not have the leakage problem. However, the recent development of deep submicron processes with low V_{TH} devices are causing leakage problems even in CMOS circuits [18], [19].

The 0.13-μm process used in our design has relatively low threshold voltages of -150 mV and 200 mV for pMOS and nMOS transistors, respectively. In order to evaluate the effect

of the leakage current, we have modeled the nonidealities in Matlab/Simulink for behavioral simulation, as shown in Fig. 9. The simulation technique is well developed in [20], in which op amp slewing, finite dc gain, integrator saturation, KT/C noise, and clock jitter are all modeled. Since the previous techniques do not have a model for leakage current, the new model for leakage current is explained in this paper. Details about the modeling technique for other nonidealities can be found in [20].

Since the leakage current in the switch is not linear, we used a lookup table instead of a mathematical function. The HSPICE simulation of the switch is performed to extract the leakage current as shown in Fig. 10. It shows that up to 30-nA current can flow through the assumed turned-off switches. The leakage current is converted to the voltage level by the *I–V* converter function as shown in Fig. 11.

The behavioral simulations with nonidealities showed that the noise floor is increased to the -120 dB level. The op amp's finite dc gain moves the NTF zero from dc to a higher frequency [14], and the effects of thermal noise and clock jittering are combined to increase the noise floor. As expected, the nonlinear leakage current causes harmonic distortion in our simulation. Fig. 12 shows the simulation result with and without the leakage current. The simulation result with the leakage current clearly shows harmonic distortions.

As the leakage current becomes a problem, complex switching techniques have been proposed to prevent the leakages [19]. However, the proposed techniques use complex switches instead of simple CMOS or nMOS switches. Sometimes even the negative voltage is generated to turn off the switch completely. After careful consideration of those switches, we have decided to use simple conventional switches for circuit simplicity and power efficiency at the cost of additional harmonic distortions.

III. CIRCUIT IMPLEMENTATION

The key analog building blocks in the modulator are explained in this section. The OTA is the most critical block, and is explained first. Other important blocks are subsequently explained.

A. Low-Power High-Performance OTA

The most critical part of the delta-sigma modulator is the operational transconductance amplifiers (OTAs). In particular, the first OTA has dominant impact on modulator performance, hence, the first OTA consumes about half or sometimes more than half of the total power.

The class-AB circuit is known to be more power efficient; therefore, it is a widely used OTA architecture [2], [9]. However, a drawback of the class-AB architecture is that it requires extra circuit to provide battery voltage to control the quiescent current of the pMOS and nMOS output transistors. For accurate control of low-quiescent current consumption, a process-voltage-temperature (PVT) independent battery circuit is required, which unavoidably increases total quiescent current. To reduce extra quiescent current increase, sometimes the gate-source voltage of the source follower is used as a battery voltage [9]. This has the advantage of simple circuit design; however, it has PVT dependency, and modulator performance could vary inevitably. Our
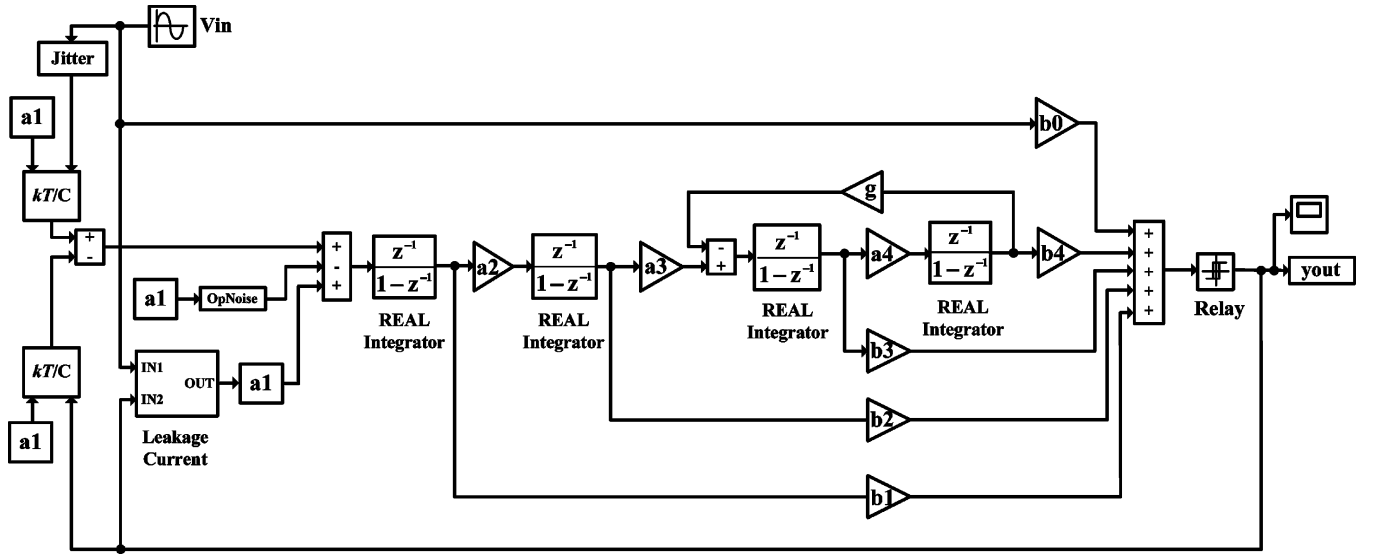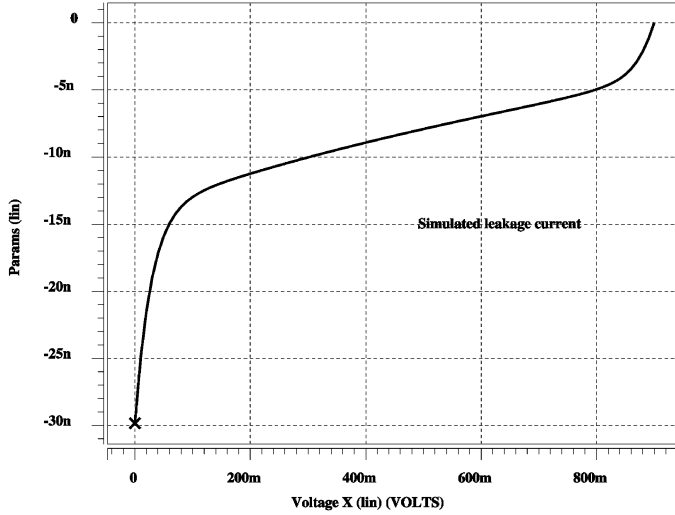
Fig. 9. Behavioral model in Simulink.

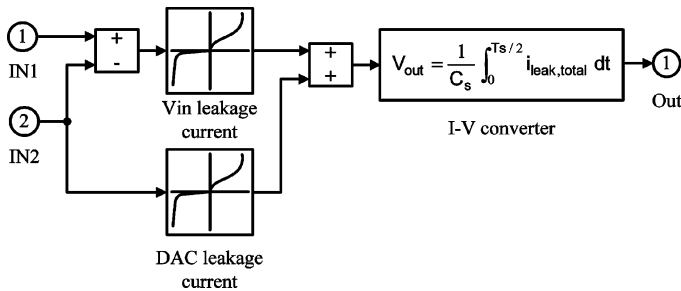Fig. 10. HSPICE simulation result of switch leakage current.

Fig. 11. Leakage current model in Simulink.

(a)

(b)

Fig. 12. Simulation results (a) with and (b) without leakage current.

design goal is to minimize power consumption; therefore, complex circuitry to implement a class-AB OTA is avoided.

Another important design criteria in an OTA is the high-gain and wide bandwidth not only for the integrator settling but also for the high power supply rejection ratio (PSRR). The folded-cascode amplifier is one of the most popular selections in delta-sigma modulators [11]. It achieves high-gain by transistor cascoding without multistage amplification. Because of
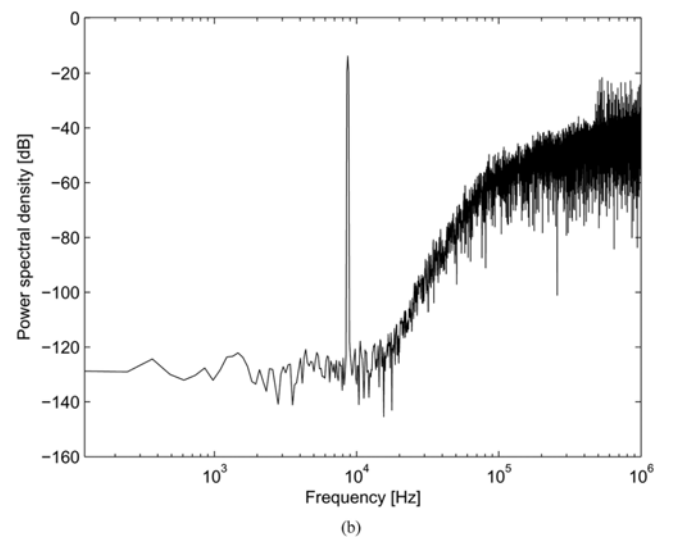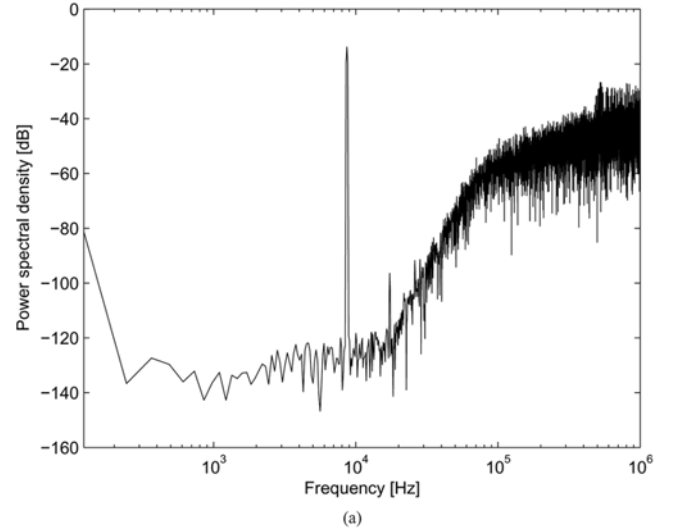
its single-stage nature, the frequency compensation is achieved by a load capacitor in a switched-capacitor circuit. However,
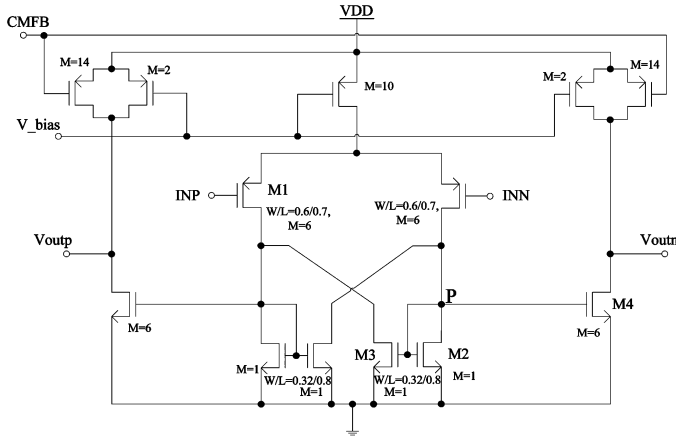
Fig. 13. Schematic of the first OTA. (NMOS unit size $W/L = 0.4/0.8$, and pMOS unit size $W/L = 2.2/2.0$ unless otherwise noted. Units are in μm).

TABLE II
SIMULATED PERFORMANCE OF THE OTAS

Parameter	OTA1	Other OTAs
Supply voltage (V)	0.9	0.9
Static supply current (μA)	22.7	5.3
DC gain (dB)	55	43
Phase margin (degree)	29	66
Load capacitor ($C_{L,eff}$) (pF)	3	0.8
GBW (MHz)	37	14
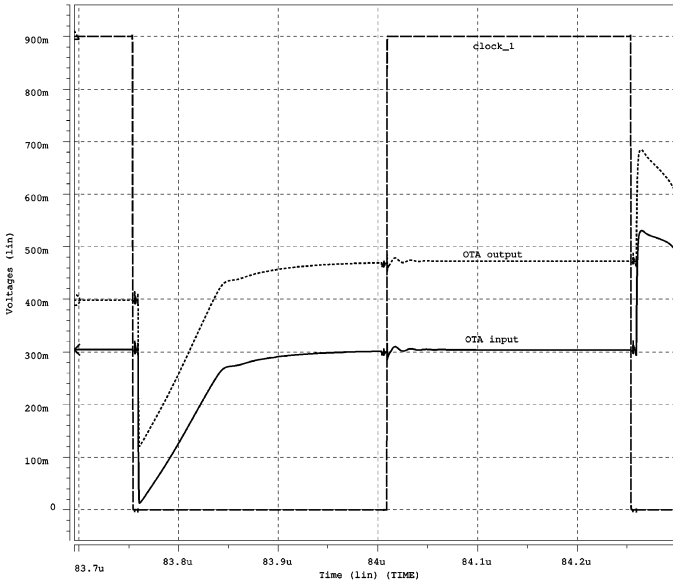
Fig. 14. First integrator's settling behavior.

Fig. 15. Schematic of a switched-capacitor CMFB circuit.
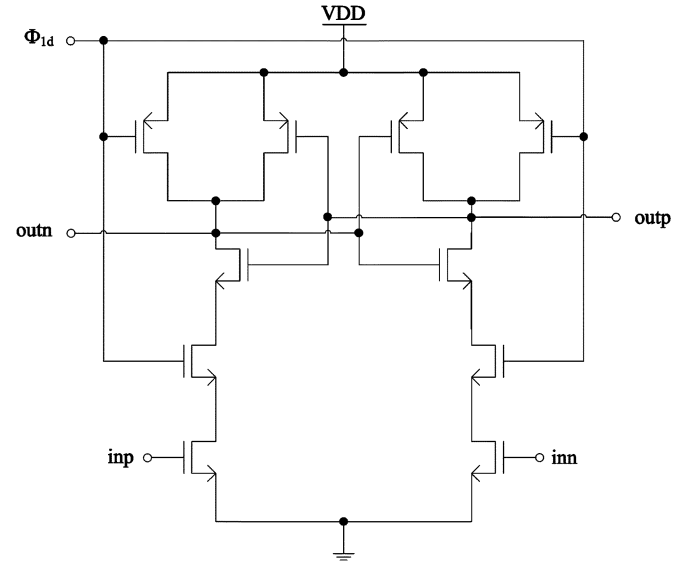
Fig. 16. Schematic of a comparator.
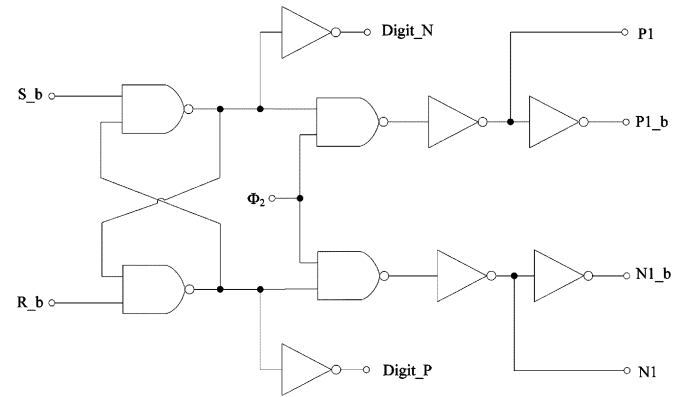
Fig. 17. Schematic of an SR latch.

transistor cascoding requires extra voltage headroom, and is usually avoided in low-voltage design.

In our circuit design, which is shown in Fig. 13, we use a simple single-stage class-A architecture with local positive feedback [15], [16] to increase amplifier gain and gain-bandwidth product (GBW) as

$$A_d = g_{m1} R_{\text{out}} \times \frac{B}{1-\alpha} \qquad (3)$$

$$\text{GBW} = \frac{g_{m1}}{2\pi C_L} \frac{B}{1-\alpha}. \qquad (4)$$

where $\alpha = (W/L)_3/(W/L)_2$, $B = (W/L)_4/(W/L)_2$, and R_{out} is the output resistance of the OTA. In the above equations, we ignore the effect of the drain-source resistances of the input pair and the current steering transistors since the resistances are large because of the small amount of current and relatively large transistor lengths. If the amount of positive feedback is larger than 1, the circuit becomes a latch. In this design, the parameters are $\alpha = 0.8$ and $B = 6$ for the first OTA. A reasonable value for α is 0.75, and a practical maximum value for α is 0.9, because beyond that any mismatches may cause the value of α to

Fig. 18. Schematic of the presented fourth-order modulator.

approach unity [16]. We have selected 0.8 as a optimum value in our design after circuit simulations with possible mismatches.

Table II shows the simulation results of the designed OTAs. In order to evaluate the performance of the OTAs in the capacitive feedback configuration, the effective load capacitances, $C_{L,\text{eff}}$, are estimated. In our circuit configuratio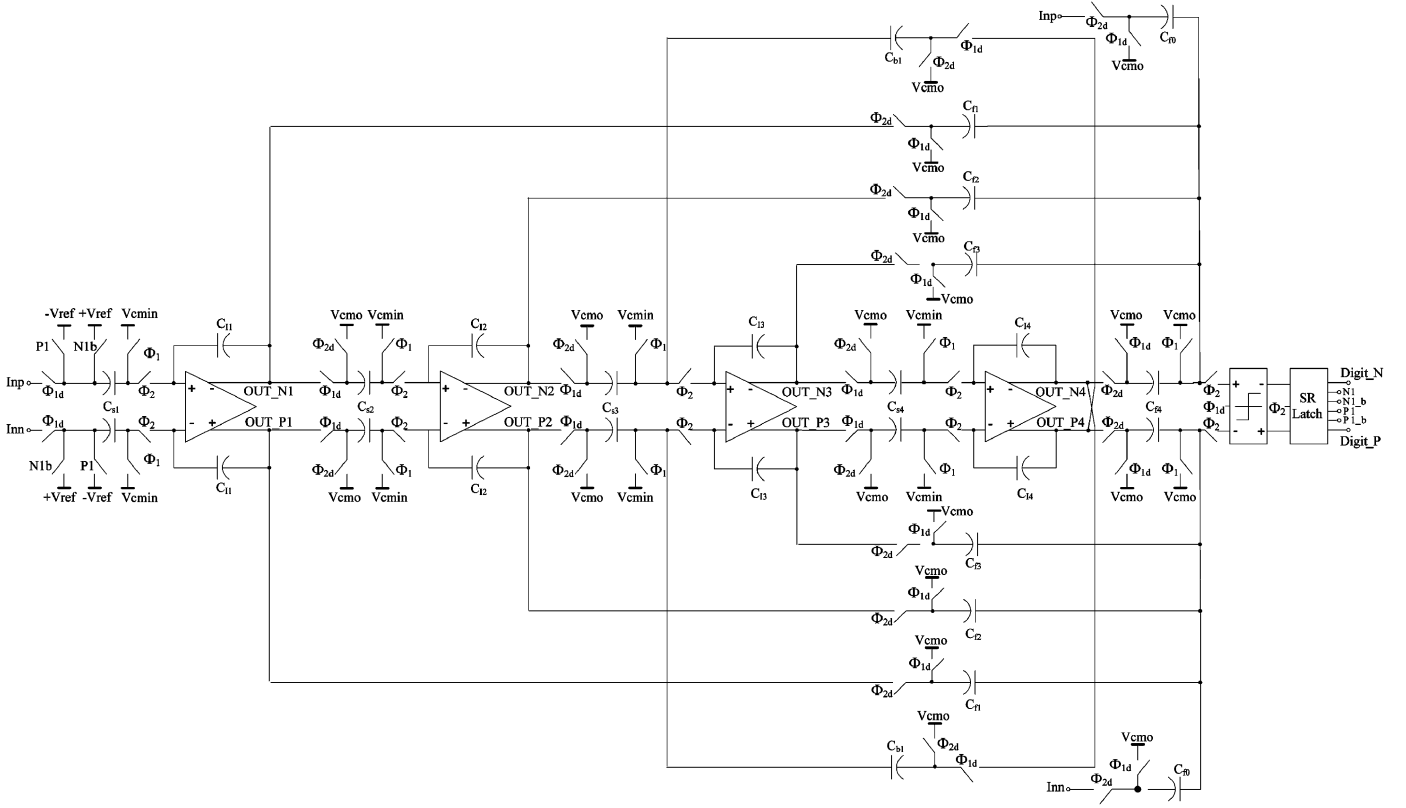n, the OTAs in the sampling phase, when $\Phi 1$ is high, have lower $C_{L,\text{eff}}$, which means that they will have a lower phase margin than in the integrating phase. The equation for $C_{L,\text{eff}}$ is shown below [14], [17]

$$C_{L,\text{eff}} = C_L + \frac{C_i \times C_p}{C_i + C_p} \tag{5}$$

where C_L is the load capacitance, C_i is the integrating capacitance, and C_p is the parasitic capacitance at the OTA input node. With the estimated effective load capacitance of 3 pF, the first OTA has 55-dB DC gain and 37-MHz GBW, which is sufficient for our modulator, as shown in Fig. 8. With the 3-pF load capacitor, the phase margin of the first OTA is the relatively low value of 29°. During the $\Phi 1$ cycle, the first OTA drives the sampling capacitor of the second integrator, which is only 0.4 pF. Since the phase margin is low, the OTA input and output voltage have slight ringing at the beginning of the clock cycle as shown in Fig. 14. However, even though there is some ringing, we have confirmed from circuit simulation that the circuit settles with sufficient accuracy. Instead of reducing bandwidth to achieve higher phase margin, we designed the circuit to have very high speed operation with a little bit of ringing at the beginning of the clock cycle. The other OTAs are relatively less critical than

TABLE III
CAPACITANCE VALUES USED IN THE MODULATOR (UNITS ARE IN pF)

Sampling capacitors	Integrating capacitors	Feedforward capacitors	Resonator capacitor
		$C_{f0}=0.1$	
$C_{s1}=3$	$C_{i1}=15$	$C_{f1}=0.4$	$C_{b1}=0.06$
$C_{s2}=0.4$	$C_{i2}=0.8$	$C_{f2}=0.3$	
$C_{s3}=0.96$	$C_{i3}=2.16$	$C_{f3}=0.15$	
$C_{s4}=0.2$	$C_{i4}=2$	$C_{f4}=0.15$	

the first OTA; therefore, the current and performance are scaled down to reduce power consumption.

Fig. 15 shows the switched-capacitor common-mode feedback (SC-CMFB) circuit that is used for the fully-differential circuit implementation [21]. The CMFB circuit senses the output common-mode voltage and provides the control voltage to balance the OTA's positive and negative outputs. The switches are implemented using nMOS transistors except for the two switches connected to the outputs of the OTA, which are implemented as CMOS switches to accommodate wider voltage swings. The capacitor values in this circuit are 0.1 pF and 0.4 pF for C_1 and C_2, respectively.

B. Single-Bit Quantizer and SR Latch

The design requirement of a 1-bit comparator can be relaxed in delta-sigma modulators since the nonidealities of the comparator also experience noise-shaping the same as the quantization noise. The comparator in Fig. 16 uses the dynamic latch architecture controlled by a clock signal. When the Φ_{1d} signal is low, two pMOS transistors pull up the *outp* and *outn* nodes,
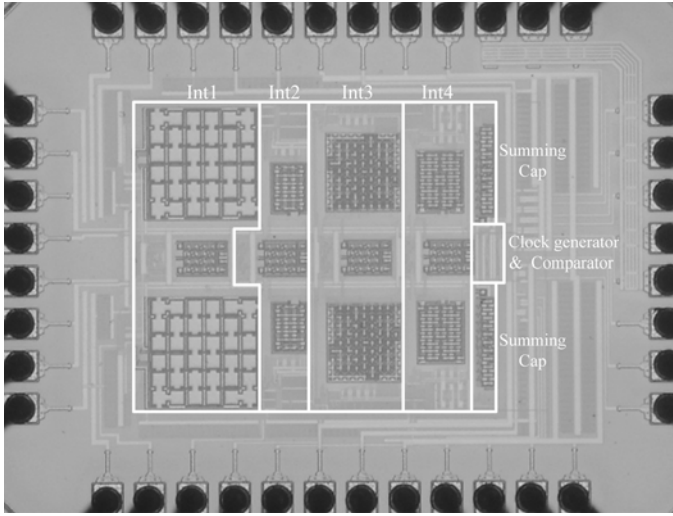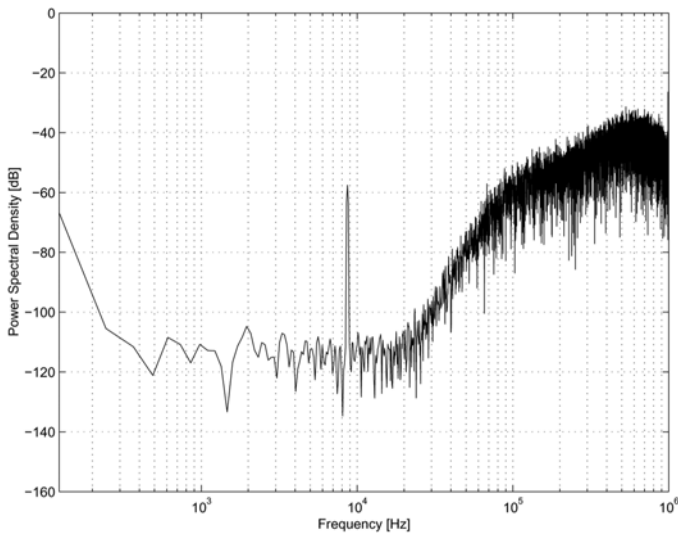
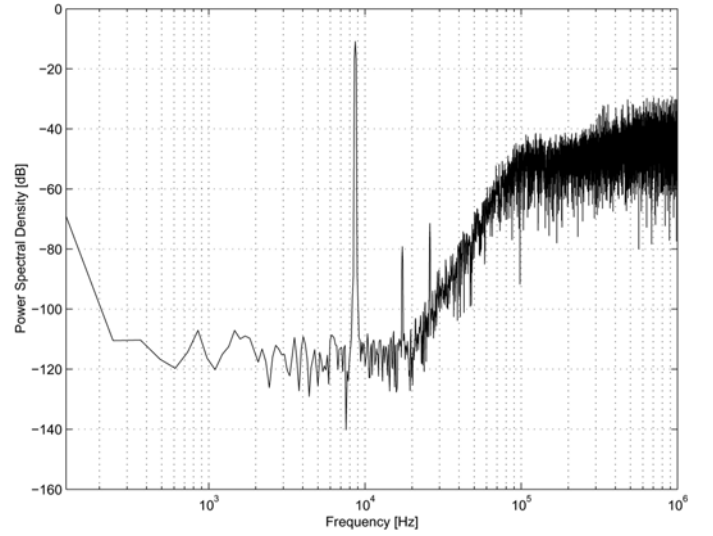Fig. 19.   Chip photograph.

Fig. 21.   Output spectrum for high amplitude input signal.

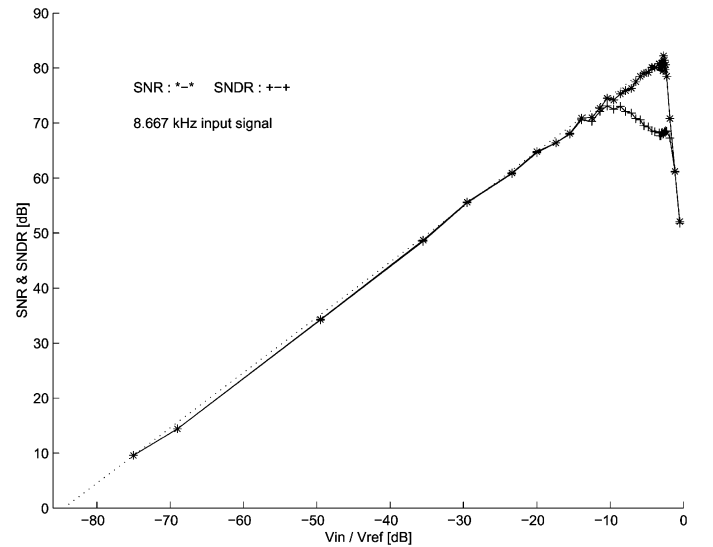Fig. 20.   Output spectrum with 16 k samples.

Fig. 22.   Measured SNR and SNDR versus input amplitude.

while the nMOS pull-down path is disconnected. At this timing, both output signals are high, which mandates the use of the SR latch following the comparator. When Φ_{1d} signal goes high, two pMOS pull-up transistors turn off, and at the same time the two nMOS transistors turn on. Now the *outp* and *outn* nodes experience voltage drops from the power supply. The speed of the voltage drop is determined by the input voltage of the comparator. Because of the positive latch in the comparator, the regenerative process begins to speed up the comparator decision.

The comparator output drives the SR latch in Fig. 17. The SR latch stores the comparison result during the pull-up phase of the comparator, and controls the feedback DAC timing. The $P1$, $N1$, and their respective inverting signals control the feedback signal as shown in Fig. 18. They drive the switches that connect either the positive supply voltage or ground as the 1-bit DAC feedback voltage. The timing is synchronized with Φ_2 for

TABLE IV
PERFORMANCE SUMMARY

Supply voltage	0.9 V
Analog power consumption	55 μW
Digital power consumption	5 μW
Peak SNR	82.2 dB
Peak SNDR	73.1 dB
Dynamic range	83 dB
Sampling frequency	2 MHz
Signal bandwidth	20 kHz
Oversampling ratio	50
Core size	0.42 mm^2
Figure of merit	168

the integrator operation. The Digit_N and Digit_P signals are connected to the digital output pads, which generate the modulator output captured by the logic analyzer for further analysis.

TABLE V
PERFORMANCE COMPARISON OF SUB-1-V DELTA-SIGMA MODULATORS

Paper	Supply voltage (V)	Process (μm)	DR (dB)	SNDR (dB)	BW (kHz)	Power (μW)	FOM
[2] (Peluso, 1998)	0.9	0.5	77	62	16	40	163
[3] (Sauerbrey, 2002)	0.7	0.18	75	67	8	80	155
[4] (Ahn, 2005)	0.6	0.35	79	78	20	1000	152
[5] (Goes, 2006)	0.9	0.18	83	80	10	200	165
[6] (Pun, 2007)	0.5	0.18	76	74	25	300	155
This work	0.9	0.13	83	73	20	60	168

C. Complete Modulator Circuit

The complete modulator circuit is shown in Fig. 18. It has four integrators with a comparator and a latch. We have used two kinds of common-mode voltages. The input common-mode voltage is set to 0.3 V while the output common-mode voltage is set to the middle of the power supply voltage. The input common-mode voltage is lowered to give the OTA input differential pair sufficient voltage operating room.

The power supply rails, V_{DD} and ground, are used as the feedback reference voltages $+V_{\mathrm{ref}}$ and $-V_{\mathrm{ref}}$. Two separate reference voltage pins with 10-μF and 0.1-μF decoupling capacitors are used to suppress noise interference [13].

The capacitor values are summarized in Table III. The capacitor value of the first integrator is chosen to satisfy the KT/C noise requirement as shown below [13]

$$C_s = \frac{8KT(DR)}{V_{\mathrm{DD}}{}^2 M} \qquad (6)$$

where T is the absolute temperature, DR is the dynamic range, M is the oversampling ratio, and V_{DD} is used as the amplitude of a full-scale sinusoidal input. The oversampling ratio M is 50 in our design, and the DR is set to 95 dB for a design margin. For the power supply V_{DD} of 0.9 V, the required capacitance is calculated as 2.6 pF. With the extra noise margin, the final sampling capacitance is selected as 3 pF. The other capacitors are selected to satisfy the modulator coefficients in Table I. The second and the fourth integrators have small sampling capacitors, as shown in Table III. The third integrator has another input path, which is the local resonator with a coefficient value of only 1/36. In order to implement this small ratio, the size of the resonator capacitor is chosen to be 0.06 pF and the integrating capacitor as 2.16 pF. Then, the third sampling capacitor is decided as 0.96 pF for the integrator gain of 0.44. If we try to reduce the sampling capacitor further, the resonator capacitor becomes too small, so the sampling and integrating capacitors of the third integrator look larger than those of the second and the fourth integrators.

IV. MEASUREMENT RESULTS

The designed modulator was implemented in a 0.13-μm standard CMOS process, and the fabricated chip is shown in Fig. 19. The threshold voltages of the pMOS and nMOS transistors are -150 and 200 mV, respectively. The die photo shows four operational amplifiers with their respective sampling and integrating capacitors on the top and bottom sides of the amplifier.

Capacitors are laid out in symmetry to match the signal path of the positive and negative inputs and outputs of the fully differential circuit. The capacitors in the first integrator are laid out with 750-fF unit capacitors. The second and fourth integrators

have 50-fF unit capacitors, and the third one has 60-fF unit capacitors. The level shifters and output buffers are shown on the right side of the floor plan. They are used to interface with 3-V logics on the test board.

The output spectrums of the modulator with 16 k samples are shown in Figs. 20 and 21 with 8.667-kHz sinusoidal inputs. The noise floor is increased than in the behavioral simulation, which shows that more nonidealities such as the component mismatches and the power line noise are included in the circuit operation and measurements. As the amplitude of the input signal becomes higher, harmonic distortions appear in the spectrum.

The measured SNR and SNDR curves are shown in Fig. 22, with the input amplitude normalized by the reference voltage. The peak SNR and SNDR reach 82.2 dB and 73.1 dB, respectively. The dynamic range is measured as 83 dB with power consumption of 60 μW. The measurement results are summarized in Table IV.

The performance of our modulator is compared with other state-of-the-art sub-1-V modulators in Table V. To compare performances, the common FOM equation [14] is used, which is shown below.

$$\mathrm{FOM} = DR_{\mathrm{dB}} + 10\log\left(\frac{BW}{P}\right). \qquad (7)$$

The presented modulator shows the highest FOM among the modulators. The high FOM can be explained by several reasons. The low-voltage swings of the modulator caused by the feedforward architecture make the OTA circuits very power-efficient. With very low output swing, low-quiescent current OTA is designed without concern for slewing. Another reason comes from the simplicity of our circuit components. Our design does not include charge pumps, switched-op amps, or switched-RC integrators, which may require extra control circuits and extra current.

V. CONCLUSION

A very low-power delta-sigma modulator is implemented in a 0.13-μm CMOS process. Input feedforward modulator architecture is used to reduce the voltage swings of the integrators. By reducing the integrator swings, more power-efficient OTAs can be used for low-power circuit design. The issues of parasitic integrator and switch leakage current are discussed. The circuit components are carefully laid out to minimize noise interference. The measurement results show that this modulator can be used for very low-power audio and sensor applications. The FOM comparison among the sub-1-V modulators proves that the presented modulator has highly optimized performance.

REFERENCES

[1] J. C. Candy and G. C. Temes, *Oversampling Delta-Sigma Data Converters: Theory, Design and Simulation*. Piscataway, NJ: IEEE Press, 1992.

[2] V. Peluso, P. Vancorenland, A. M. Marques, M. S. J. Steyaert, and W. Sansen, "A 900-mV low-power $\Delta\Sigma$ A/D converter with 77-dB dynamic range," *IEEE J. Solid-State Circuits*, vol. 33, no. 12, pp. 1887–1897, Dec. 1998.

[3] J. Sauerbrey, T. Tille, D. Schmitt-Landsiedel, and R. Thewes, "A 0.7-V MOSFET-only switched-opamp $\Delta\Sigma$ modulator in standard digital CMOS technology," *IEEE J. Solid-State Circuits*, vol. 37, no. 12, pp. 1662–1669, Dec. 2002.

[4] G.-C. Ahn, D.-Y. Chang, M. E. Brown, N. Ozaki, H. Youra, K. Yamamura, K. Hamashita, K. Takasuka, G. C. Temes, and U. Moon, "A 0.6-V 82-dB delta-sigma audio ADC using switched-RC integrators," *IEEE J. Solid-State Circuits*, vol. 40, no. 12, pp. 2398–2407, Dec. 2005.

[5] J. Goes, B. Vaz, R. Monteiro, and N. Paulino, "A 0.9 V $\Delta\Sigma$ modulator with 80 dB SNDR and 83 dB DR using a single-phase technique," in *IEEE ISSCC Dig. Tech. Papers*, 2006, pp. 74–75.

[6] K.-P. Pun, S. Chatterjee, and P. R. Kinget, "A 0.5-V 74-dB SNDR 25-kHz continuous-time delta-sigma modulator with a return-to-open DAC," *IEEE J. Solid-State Circuits*, vol. 42, no. 3, pp. 496–507, Mar. 2007.

[7] M. Dessouky and A. Kaiser, "Very low-voltage digital-audio $\Delta\Sigma$ modulator with 88-dB dynamic range using local switch bootstrapping," *IEEE J. Solid-State Circuits*, vol. 36, no. 3, pp. 349–355, Mar. 2001.

[8] S. S. Bazarjani, M. Snelgrove, and T. MacElwee, "A 1 V switched-capacitor $\Sigma\Delta$ modulator," in *Proc. IEEE Symp. Low Power Electronics*, Oct. 1995, pp. 70–71.

[9] L. Yao, M. Steyaert, and W. Sansen, "A 1-V 140- μW 88-dB audio sigma-delta modulator in 90-nm CMOS," *IEEE J. Solid-State Circuits*, vol. 39, no. 11, pp. 1809–1818, Nov. 2004.

[10] J. Silva, U. Moon, J. Steensgaard, and G. C. Temes, "Wideband low-distortion delta-sigma ADC topology," *IEE Electron. Lett.*, vol. 37, no. 6, pp. 737–738, Jun. 2001.

[11] Y. Yang, A. Chokhawala, M. Alexander, J. Melanson, and D. Hester, "A 114-dB 68-mW chopper-stabilized stereo multibit audio ADC in 5.62 mm^2," *IEEE J. Solid-State Circuits*, vol. 38, no. 12, pp. 2061–2068, Dec. 2003.

[12] A. Gharbiya and D. A. Johns, "On the implementation of input-feed-forward delta-sigma modulators," *IEEE Trans. Circuits Syst. II, Exp. Briefs*, vol. 53, no. 6, pp. 453–457, Jun. 2006.

[13] S. Rabii and B. A. Wooley, *The Design of Low-Voltage, Low-Power Sigma-Delta Modulators*. Norwell, MA: KAP, 1999.

[14] R. Schreier and G. C. Temes, *Understanding Delta-Sigma Data Converters*. Piscataway, NJ: IEEE Press, 2005.

[15] K. B. Ohri and M. J. Callahan, Jr, "Integrated PCM codec," *IEEE J. Solid-State Circuits*, vol. SC-14, no. 1, pp. 38–46, Feb. 1979.

[16] R. Gregorian, *Introduction to CMOS Op-Amps and Comparators*. New York: Wiley, 1999.

[17] J. Adut, J. Silva-Martinez, and M. Rocha-Perez, "A 10.7-MHz sixth-order SC ladder filter in 0.35-μm CMOS technology," *IEEE Trans. Circuits Syst. I, Reg. Papers*, vol. 53, pp. 1625–1635, Aug. 2006.

[18] K. Roy, S. Mukhopadhyay, and H. Mahmoodi-Meimand, "Leakage current mechanisms and leakage reduction techniques in deep-submicrometer CMOS circuits," *Proc. IEEE*, vol. 91, no. 2, pp. 305–327, Feb. 2003.

[19] K. Ishida, K. Kanda, A. Tamtrakarn, H. Kawaguchi, and T. Sakurai, "Managing subthreshold leakage in charge-based analog circuits with low-V_{TH} transistors by analog T-switch (AT-switch) and super cut-off CMOS (SCCMOS)," *IEEE J. Solid-State Circuits*, vol. 41, no. 4, pp. 859–867, Apr. 2006.

[20] P. Malcovati, S. Brigati, F. Francesconi, F. Maloberti, and A. Baschirotto, "Behavioral modeling of switched-capacitor sigma-delta modulators," *IEEE Trans. Circuits Syst. I, Fundam. Theory Appl.*, vol. 50, pp. 352–364, Mar. 2003.

[21] D. Senderowicz, S. F. Dreyer, J. H. Huggins, C. F. Rahim, and C. A. Laber, "A family of differential nMOS analog circuits for a PCM codec filter chip," *IEEE J. Solid-State Circuits*, vol. SC-17, no. 6, pp. 1982–1023, Dec. 1982.
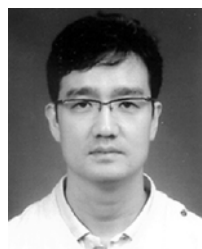
Jeongjin Roh (M'01) received the B.S. degree in electrical engineering from Hanyang University, Seoul, Korea, in 1990, the M.S. degree in electrical engineering from the Pennsylvania State University, University Park, in 1998, and the Ph.D. degree in computer engineering from the University of Texas at Austin in 2001.

From 1990 to 1996, he was with Samsung Electronics, Kiheung, Korea, as a Senior Circuit Designer for several mixed-signal products. From 2000 to 2001, he was with Intel Corporation, Austin, TX, as a Senior Analog Designer for delta-sigma data converters. In 2001, he joined the faculty of Hanyang University, Ansan, Korea. His research interests include oversampled delta-sigma converters and power management circuits.
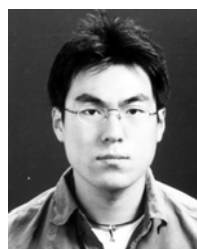
Sanho Byun received the B.S. and M.S. degrees in electrical engineering and computer science from Hanyang University, Ansan, Korea, in 2005 and 2007, respectively.

He subsequently joined Samsung Electronics Corporation, Giheung, Korea. Since then, he has been engaged in the research and development of LSI design for display.

Youngkil Choi (S'06) received the B.S. and M.S. degrees in electrical engineering and computer science from Hanyang University, Ansan, Korea, in 2004 and 2006, respectively, where he is currently working towards the Ph.D. degree in electrical engineering and computer science.

His research interests include low-power high-performance sigma-delta modulators and mixed-signal integrated circuits.

Hyungdong Roh (S'06) received the B.S. and M.S. degrees in electrical engineering and computer science from Hanyang University, Ansan, Korea, in 2005 and 2007, respectively, where he is currently pursuing the Ph.D. degree.

His current research interest is low-voltage and low-power sigma-delta A/D converters.

Yi-Gyeong Kim was born in Busan, Korea, in 1976. He received the B.S. degree in electronic, electric and communication engineering from Pusan National University, Busan, Korea, in 2003, and the M.S. degree in electrical engineering from Korea Advanced Institute of Science and Technology (KAIST), Daejeon, Korea, in 2005.

He subsequently joined Electronics and Telecommunications Research Institute (ETRI), Daejeon, Korea, where he is a Member of Engineering Staff. His main research interests are in the design of mixed-signal integrated circuits, including sigma-delta data converters and Nyquist-rate data converters.

Jong-Kee Kwon (M'96) received the B.S and M.S. degrees in electronics engineering from Yeungnam University, Korea, in 1981 and 1983, respectively, and the Ph.D. degree in electrical engineering from Korea Advanced Institute of Science and Technology (KAIST), Daejeon, Korea, in 2004.

Since 1984, he has been with Electronics and Telecommunications Research Institute (ETRI), Daejeon, Korea, working mainly on the development of analog integrated circuits (ICs). As the Technical Manager of the Mixed-Signal Product Engineering Department at ETRI, he currently is involved in the development of high-speed, high performance mixed-signal ICs including low voltage/low power analog functions; amplifiers, high-speed/high-resolution data converters, PLL/VCO, and analog interfaces for sensor or MEMS systems.